Eur. Phys. J. C 30, 145–158 (2003)
Digital Object Identifier (DOI) 10.1140/epjc/s2003-01291-4

THE EUROPEAN
PHYSICAL JOURNAL C

Measurement of the hadronic photon structure function $F_2^\gamma(x, Q^2)$ in two-photon collisions at LEP

The ALEPH Collaboration

A. Heister, S. Schael
Physikalisches Institut das RWTH-Aachen, 52056 Aachen, Germany

R. Barate, R. Brunelière, I. De Bonis, D. Decamp, C. Goy, S. Jezequel, J.-P. Lees, F. Martin, E. Merle, M.-N. Minard, B. Pietrzyk, B. Trocmé
Laboratoire de Physique des Particules (LAPP), IN^{2}P^3-CNRS, 74019 Annecy-le-Vieux Cedex, France

S. Bravo, M.P. Casado, M. Chmeissani, J.M. Crespo, E. Fernandez, M. Fernandez-Bosman, Ll. Garrido[15], M. Martinez, A. Pacheco, H. Ruiz
Institut de Física d'Altes Energies, Universitat Autònoma de Barcelona, 08193 Bellaterra (Barcelona), Spain[7]

A. Colaleo, D. Creanza, N. De Filippis, M. de Palma, G. Iaselli, G. Maggi, M. Maggi, S. Nuzzo, A. Ranieri, G. Raso[24], F. Ruggieri, G. Selvaggi, L. Silvestris, P. Tempesta, A. Tricomi[3], G. Zito
Dipartimento di Fisica, INFN Sezione di Bari, 70126 Bari, Italy

X. Huang, J. Lin, Q. Ouyang, T. Wang, Y. Xie, R. Xu, S. Xue, J. Zhang, L. Zhang, W. Zhao
Institute of High Energy Physics, Academia Sinica, Beijing, P.R. China[8]

D. Abbaneo, T. Barklow[26], O. Buchmüller[26], M. Cattaneo, B. Clerbaux[23], H. Drevermann, R.W. Forty, M. Frank, F. Gianotti, J.B. Hansen, J. Harvey, D.E. Hutchcroft[30], P. Janot, B. Jost, M. Kado[2], P. Mato, A. Moutoussi, F. Ranjard, L. Rolandi, D. Schlatter, G. Sguazzoni, F. Teubert, A. Valassi, I. Videau
European Laboratory for Particle Physics (CERN), 1211 Geneva 23, Switzerland

F. Badaud, S. Dessagne, A. Falvard[20], D. Fayolle, P. Gay, J. Jousset, B. Michel, S. Monteil, D. Pallin, J.M. Pascolo, P. Perret
Laboratoire de Physique Corpusculaire, Université Blaise Pascal, IN^{2}P^3-CNRS, Clermont-Ferrand, 63177 Aubière, France

J.D. Hansen, J.R. Hansen, P.H. Hansen, A.C. Kraan, B.S. Nilsson
Niels Bohr Institute, 2100 Copenhagen, Denmark[9]

A. Kyriakis, C. Markou, E. Simopoulou, A. Vayaki, K. Zachariadou
Nuclear Research Center Demokritos (NRCD), 15310 Attiki, Greece

A. Blondel[12], J.-C. Brient, F. Machefert, A. Rougé, H. Videau
Laoratoire Leprince-Ringuet, Ecole Polytechnique, IN^{2}P^3-CNRS, 91128 Palaiseau Cedex, France

V. Ciulli, E. Focardi, G. Parrini
Dipartimento di Fisica, Università di Firenze, INFN Sezione di Firenze, 50125 Firenze, Italy

A. Antonelli, M. Antonelli, G. Bencivenni, F. Bossi, G. Capon, F. Cerutti, V. Chiarella, P. Laurelli, G. Mannocchi[5], G.P. Murtas, L. Passalacqua
Laboratori Nazionali dell'INFN (LNF-INFN), 00044 Frascati, Italy

J. Kennedy, J.G. Lynch, P. Negus, V. O'Shea, A.S. Thompson
Department of Physics and Astronomy, University of Glasgow, Glasgow G12 8QQ, UK[10]

S. Wasserbaech
Utah Valley State College, Orem, UT 84058, USA

R. Cavanaugh[4], S. Dhamotharan[21], C. Geweniger, P. Hanke, V. Hepp, E.E. Kluge, A. Putzer, H. Stenzel, K. Tittel, M. Wunsch[19]
Kirchhoff-Institut für Physik, Universität Heidelberg, 69120 Heidelberg, Germany[16]

R. Beuselinck, W. Cameron, G. Davies, P.J. Dornan, M. Girone[1], R.D. Hill, N. Marinelli, J. Nowell, S.A. Rutherford, J.K. Sedgbeer, J.C. Thompson[14], R. White
Department of Physics, Imperial College, London SW7 2BZ, Uk[10]

V.M. Ghete, P. Girtler, E. Kneringer, D. Kuhn, G. Rudolph
Institut für Experimentalphysik, Universität Innsbruck, 6020 Innsbruck, Austria[18]

E. Bouhova-Thacker, C.K. Bowdery, D.P. Clarke, G. Ellis, A.J. Finch, F. Foster, G. Hughes, R.W.L. Jones, M.R. Pearson, N.A. Robertson, M. Smizanska
Department of Physics, University of Lancaster, Lancaster LA1 4YB, UK[10]

O. van der Aa, C. Delaere[28], G.Leibenguth[31], V. Lemaitre[29]
Institut de Physique Nucléaire, Département de Physique, Université Catholique de Louvain, 1348 Louvain-la-Neuve, Belgium

U. Blumenschein, F. Hölldorfer, K. Jakobs, F. Kayser, K. Kleinknecht, A.-S. Müller, B. Renk, H.-G. Sander, S. Schmeling, H. Wachsmuth, C. Zeitnitz, T. Ziegler
Institut für Physik, Universität Mainz, 55099 Mainz, Germany[16]

A. Bonissent, P. Coyle, C. Curtil, A. Ealet, D. Fouchez, P. Payre, A. Tilquin
Centre de Physique des Particules de Marseille, Univ Méditerranée, IN^{2}P^3-CNRS, 13288 Marseille, France

F. Ragusa
Dipartimento di Fisica, Università di Milano e INFN Sezione di Milano, 20133 Milano, Italy

A. David, H. Dietl, G. Ganis[27], K. Hüttmann, G. Lütjens, W. Männer, H.-G. Moser, R. Settles, M. Villegas, G. Wolf
Max-Planck-Institut für Physik, Werner-Heisenberg-Institut, 80805 München, Germany[16]

J. Boucrot, O. Callot, M. Davier, L. Duflot, J.-F. Grivaz, Ph. Heusse, A. Jacholkowska[6], L. Serin, J.-J. Veillet
Laboratoire de l'Accélérateur Linéaire, Université de Paris-Sud, IN^{2}P^3-CNRS, 91898 Orsay Cedex, France

P. Azzurri, G. Bagliesi, T. Boccali, L. Foà, A. Giammanco, A. Giassi, F. Ligabue, A. Messineo, F. Palla, G. Sanguinetti, A. Sciabà, P. Spagnolo R. Tenchini A. Venturi P.G. Verdini
Dipartimento di Fisica dell'Università, INFN Sezione di Pisa, e Scuola Normale Superiore, 56010 Pisa, Italy

O. Awunor, G.A. Blair, G. Cowan, A. Garcia-Bellido, M.G. Green, L.T. Jones, T. Medcalf, A. Misiejuk, J.A. Strong, P. Teixeira-Dias
Department of Physics, Royal Holloway & Bedford New College, University of London, Egham, Surrey TW20 OEX, UK[10]

R.W. Clifft, T.R. Edgecock, P.R. Norton, I.R. Tomalin, J.J. Ward
Particle Physics Dept., Rutherford Appleton Laboratory, Chilton, Didcot, Oxon OX11 OQX, UK[10]

B. Bloch-Devaux, D. Boumediene, P. Colas, B. Fabbro, E. Lançon, M.-C. Lemaire, E. Locci, P. Perez, J. Rander, B. Tuchming, B. Vallage
CEA, DAPNIA/Service de Physique des Particules, CE-Saclay, 91191 Gif-sur-Yvette Cedex, France[17]

A.M. Litke, G. Taylor
Institute for Particle Physics, University of California at Santa Cruz, Santa Cruz, CA 95064, USA[22]

C.N. Booth, S. Cartwright, F. Combley[25], P.N. Hodgson, M. Lehto, L.F. Thompson
Department of Physics, University of Sheffield, Sheffield S3 7RH, UK[10]

A. Böhrer, S. Brandt, C. Grupen, J. Hess, A. Ngac, G. Prange
Fachbereich Physik, Universität Siegen, 57068 Siegen, Germany[16]

C. Borean, G. Giannini
Dipartimento di Fisica, Università di Trieste e INFN Sezione di Trieste, 34127 Trieste, Italy

H. He, J. Putz, J. Rothberg
Experimental Elementary Particle Physics, University of Washington, Seattle, WA 98195, USA

S.R. Armstrong, K. Berkelman, K. Cranmer, D.P.S. Ferguson, Y. Gao[13], S. González, O.J. Hayes, H. Hu, S. Jin, J. Kile, P.A. McNamara III, J. Nielsen, Y.B. Pan, J.H. von Wimmersperg-Toeller, W. Wiedenmann, J. Wu, Sau Lan Wu, X. Wu, G. Zobernig
Department of Physics, University of Wisconsin, Madison, WI 53706, USA[11]

G. Dissertori
Institute for Particle Physics, ETH Hönggerberg, 8093 Zürich, Switzerland

Received: 12 June 2003 /

Abstract. The hadronic photon structure function $F_2^\gamma(x,Q^2)$ is measured from data taken with the ALEPH detector at LEP. At centre-of-mass energies between $\sqrt{s} = 189\,\mathrm{GeV}$ and $207\,\mathrm{GeV}$ an integrated luminosity of $548.4\,\mathrm{pb}^{-1}$ is analyzed in two ranges of Q^2 with $\langle Q^2\rangle = 17.3\,\mathrm{GeV}^2$ and $67.2\,\mathrm{GeV}^2$. Detector effects and acceptance are corrected for with a Tikhonov unfolding procedure. The results are compared to theoretical predictions and measurements from other experiments.

1 Introduction

The hadronic structure function F_2^γ plays an important role in the description of the hadronic nature of the photon. It is a function of the Bjorken variable x which in leading order gives the fractional momentum of the resolved parton in the target photon, and also a function of the virtualities Q^2 and P^2 of the two interacting photons. In this measurement two-photon events are used where one of the scattered electrons is detected ('tagged') in the luminosity calorimeters and the second one remains undetected, since the scattering angle is too small and the electron escapes along the beam pipe. For these single-tag events the virtuality P^2 of the photon radiated from the undetected electron is small. This photon is considered as a quasi-real target photon that is probed by the highly virtual photon from the tagged electron. In this case the differential cross section for hadron production simplifies and only depends on the structure functions F_2^γ and F_L^γ. It is given by [1]

$$\frac{\mathrm{d}^3\sigma}{\mathrm{d}x\mathrm{d}y\mathrm{d}Q^2} = \frac{4\pi\alpha^2}{Q^4 x}\left(1 - y + \frac{y^2}{2}\right) \times \left[F_2^\gamma(x,Q^2) - \frac{y^2}{2(1-y-\frac{y^2}{2})}F_L^\gamma(x,Q^2)\right] \times \Phi(x,y) \tag{1}$$

where

$$Q^2 = -q^2 = 2E_{\mathrm{beam}}E_{\mathrm{tag}}(1 - \cos\Theta_{\mathrm{tag}}) \tag{2}$$

is the negative squared four-momentum of the virtual photon, E_{tag} and Θ_{tag} are the energy and scattering angle of the tagged beam electron, and α is the fine structure constant. The Bjorken variable x is given by

$$x = \frac{Q^2}{2p\cdot q} = \frac{Q^2}{Q^2 + W^2} \quad , \tag{3}$$

with the four-momenta q and p of the interacting photons and the total invariant mass W of the hadronic final state ($P^2 = -p^2 \ll Q^2$). The inelasticity y is given by

$$y = \frac{q\cdot p}{k\cdot p} = 1 - \frac{E_{\mathrm{tag}}}{2E_{\mathrm{beam}}}(1 + \cos\Theta_{\mathrm{tag}}) \tag{4}$$

where k is the four-momentum of the incident beam electron that is tagged. The flux function $\Phi(x,y)$ of the photons radiated from the untagged beam electron is given in [1].

---

[1] Also at CERN, 1211 Geneva 23, Switzerland

[2] Now at Fermilab, PO Box 500, MS 352, Batavia, IL 60510, USA

[3] Also at Dipartimento di Fisica di Catania and INFN Sezione di Catania, 95129 Catania, Italy

[4] Now at University of Florida, Department of Physics, Gainesville, Florida 32611-8440, USA

[5] Also Istituto di Cosmo-Geofisica del C.N.R., Torino, Italy

[6] Also at Groupe d'Astroparticules de Montpellier, Université de Montpellier II, 34095, Montpellier, France

[7] Supported by CICYT, Spain

[8] Supported by the National Science Foundation of China

[9] Supported by the Danish Natural Science Research Council

[10] Supported by the UK Particle Physics and Astronomy Research Council

[11] Supported by the US Department of Energy, grant DE-FG0295-ER40896

[12] Now at Departement de Physique Corpusculaire, Université de Genève, 1211 Genève 4, Switzerland

[13] Also at Department of Physics, Tsinghua University, Beijing, The People's Republic of China

[14] Supported by the Leverhulme Trust

[15] Permanent address: Universitat de Barcelona, 08208 Barcelona, Spain

[16] Supported by Bundesministerium für Bildung und Forschung, Germany

[17] Supported by the Direction des Sciences de la Matière, C.E.A

[18] Supported by the Austrian Ministry for Science and Transport

[19] Now at SAP AG, 69185 Walldorf, Germany

[20] Now at Groupe d' Astroparticules de Montpellier, Université de Montpellier II, 34095 Montpellier, France

[21] Now at BNP Paribas, 60325 Frankfurt am Mainz, Germany

[22] Supported by the US Department of Energy, grant DE-FG03-92ER40689

[23] Now at Institut Inter-universitaire des hautes Energies (IIHE), CP 230, Université Libre de Bruxelles, 1050 Bruxelles, Belgique

[24] Also at Dipartimento di Fisica e Tecnologie Relative, Università di Palermo, Palermo, Italy

[25] Deceased

[26] Now at SLAC, Stanford, CA 94309, USA

[27] Now at INFN Sezione di Roma II, Dipartimento di Fisica, Università di Roma Tor Vergata, 00133 Roma, Italy

[28] Research Fellow of the Belgium FNRS

[29] Research Associate of the Belgium FNRS

[30] Now at Liverpool University, Liverpool L69 7ZE, UK

[31] Supported by the Federal Office for Scientific, Technical and Cultural Affairs through the Interuniversity Attraction Pole P5/27

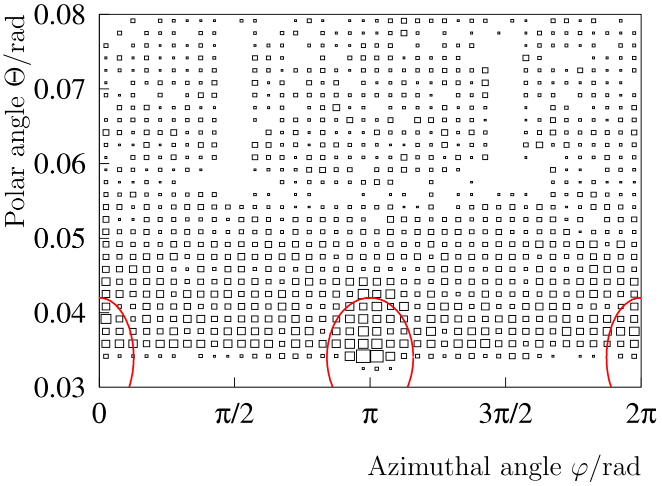

Fig. 1. Contamination of the data sample by off-momentum electrons can be seen in the (Θ, φ) plane. They are preferably radiated in the LEP plane, $\varphi \approx 0/\pi/2\pi$. The elliptic cuts are drawn as applied in the analysis

For typical experimental conditions $y \ll 1$, thus the differential cross section is not sensitive to the longitudinal structure function $F_L^\gamma(x, Q^2)$, and therefore (1) allows F_2^γ to be measured.

From Quantum Chromodynamics (QCD) it is expected that the structure function F_2^γ separates into two components as first described by Witten [2]. While the "point-like" part is calculable in perturbative QCD and shows a rise with increasing Q^2, the "hadron-like" part becomes more important for low x and is not calculable within the framework of perturbative QCD, since the photon fluctuates into a state similar to light vector mesons where the contribution of the gluon density is important. Various parametrizations of F_2^γ exist [3–12]. They differ in many aspects such as the choice of the QCD scale parameter Λ, Q^2 evolution, inclusion of heavy quark flavours, composition of hadron-like and point-like contributions and inclusion of higher order QCD corrections. Earlier calculations suffered from the limited experimental data available at the time. A very detailed review of the current status is given in [13,14].

In this paper the selection of the data sample is described after a brief introduction of the experimental setup. The Tikhonov unfolding technique is then explained followed by a discussion of the systematic uncertainties. Results are given in the last section together with a comparison to other experiments and theoretical predictions.

Table 1. Number of selected events after all cuts, listed for all centre-of-mass energies and Q^2 ranges. The range of Q^2 of the two bins analyzed is given in column three. The mean value of the virtualities $\langle Q^2 \rangle$ is calculated and listed in the fourth column. No background has been subtracted at this stage

E_{cms} /GeV	Luminosity /pb^{-1}	Number of events	Q^2 range /GeV^2	$\langle Q^2 \rangle$ /GeV^2
189	177.0	5411	10-27	16.1
		3537	27-250	61.7
196	82.6	2577	10-28	16.7
		1643	28-250	65.7
200	87.8	2694	10-29	17.4
		1648	29-250	68.3
205-207	201.0	6167	10-32	18.4
		3560	32-250	72.9
$\sum$	548.4	16849	$\langle Q^2 \rangle = 17.3\,\mathrm{GeV}^2$	
		10388	$\langle Q^2 \rangle = 67.2\,\mathrm{GeV}^2$	

Table 2. Contamination of the selected data sample through background processes

Process	Contamination [%]			
	$\langle Q^2 \rangle = 17.3\,\mathrm{GeV}^2$			
	189 GeV	196 GeV	200 GeV	205 − 207 GeV
$\gamma\gamma \to \mathrm{e^+e^-}$	0.22±0.03	0.26±0.05	0.25±0.05	0.27±0.09
$\gamma\gamma \to \mu^+\mu^-$	< 0.1			
$\gamma\gamma \to \tau^+\tau^-$	3.4±0.1	3.9±0.1	4.1±0.1	4.3±0.1
$\mathrm{e^+e^-} \to \mathrm{q\bar{q}}$	0.24±0.01	0.23±0.01	0.24±0.01	0.22±0.01
$\mathrm{e^+e^-} \to \mu^+\mu^-$	< 0.1			
$\mathrm{e^+e^-} \to \tau^+\tau^-$	< 0.1			
$\mathrm{e^+e^-} \to \mathrm{We}\nu$	< 0.1			
$\mathrm{e^+e^-} \to \mathrm{Zee}$	0.15±0.01	0.14±0.01	0.16±0.01	0.15±0.01
Q^2 migration	4.97±0.06	4.17±0.05	3.80±0.05	2.50±0.04
	$\langle Q^2 \rangle = 67.2\,\mathrm{GeV}^2$			
	189 GeV	196 GeV	200 GeV	205 − 207 GeV
$\gamma\gamma \to \mathrm{e^+e^-}$	0.3±0.04	0.22±0.05	0.31±0.07	0.41±0.14
$\gamma\gamma \to \mu^+\mu^-$	< 0.1			
$\gamma\gamma \to \tau^+\tau^-$	6.1±0.2	6.6±0.2	7.1±0.2	7.0±0.2
$\mathrm{e^+e^-} \to \mathrm{q\bar{q}}$	0.88±0.02	0.91±0.02	0.93±0.02	0.98±0.03
$\mathrm{e^+e^-} \to \mu^+\mu^-$	< 0.1			
$\mathrm{e^+e^-} \to \tau^+\tau^-$	< 0.1			
$\mathrm{e^+e^-} \to \mathrm{We}\nu$	< 0.1			
$\mathrm{e^+e^-} \to \mathrm{Zee}$	0.61±0.01	0.55±0.02	0.58±0.02	0.62±0.02
Q^2 migration	1.72±0.04	1.63±0.04	1.79±0.04	2.35±0.05

2 The ALEPH detector

A detailed description of the ALEPH detector and its performance can be found in [15,16]. The central part of the ALEPH detector is dedicated to the reconstruction of the trajectories of charged particles. The trajectory of a charged particle emerging from the interaction point is measured by a two-layer silicon strip vertex detector (VDET), a cylindrical drift chamber (ITC) and a large time projection chamber (TPC). The three tracking detectors are placed in a 1.5 T axial magnetic field provided by a superconducting solenoidal coil. Together they measure charged particle transverse momenta with a resolution of $\delta p_{\mathrm{t}}/p_{\mathrm{t}} = 6 \times 10^{-4} p_{\mathrm{t}} \oplus 0.005$ (p_{t} in GeV/c). Photons are identified in the electromagnetic calorimeter (ECAL), situated between the TPC and the coil. The ECAL is a lead/proportional-tube sampling calorimeter

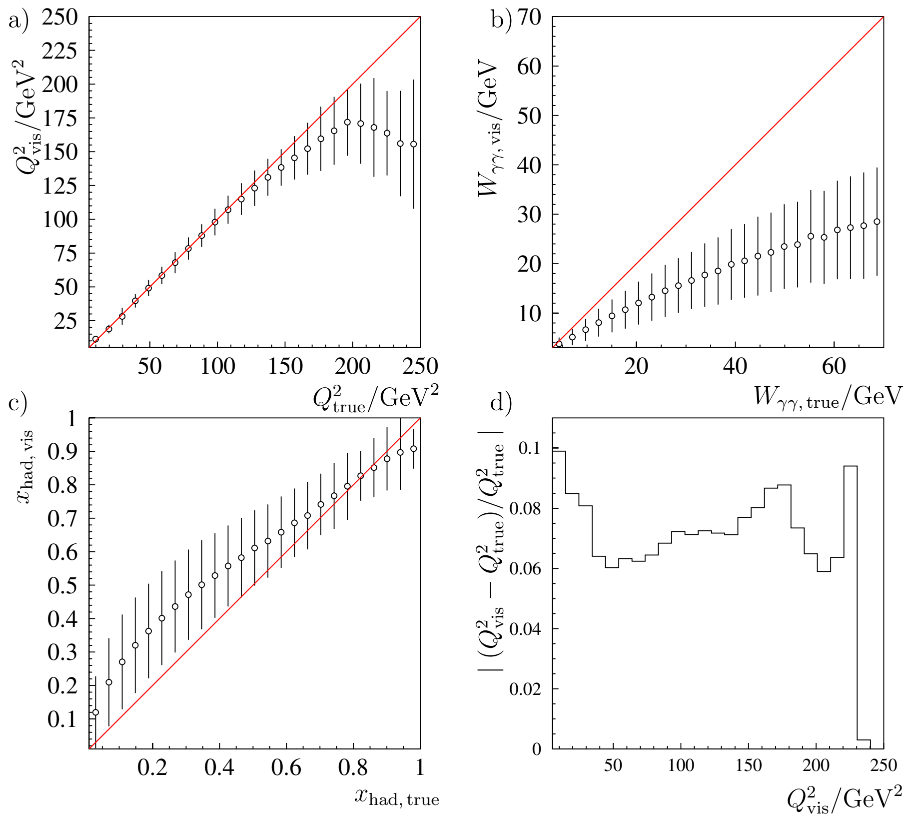

Fig. 2a–d. Comparison of the reconstructed quantity to the true values from Monte Carlo simulations; **a** the virtuality Q^2 of the probing photon, **b** the invariant hadronic mass in the final state and **c** the Bjorken variable x. The mean observed value and the standard deviation is plotted for events generated in a certain bin in the truth distribution. In **d** the relative measurement uncertainty of Q^2 is plotted as a function of the measured value of Q^2

Table 3. Statistical correlation coefficients for the results of the F_2^γ measurement. The values for the bin boundaries are given in Table 4

$\langle Q^2 \rangle = 17.3\,\mathrm{GeV}^2$									$\langle Q^2 \rangle = 67.2\,\mathrm{GeV}^2$								
x Bin	1	2	3	4	5	6	7	8	x Bin	1	2	3	4	5	6	7	8
1	1.00	-0.51	0.07	0.12	-0.08	-0.03	0.03	0.01	1	1.00	-0.48	0.01	0.20	-0.11	-0.02	0.04	-0.02
2		1.00	-0.50	-0.09	0.27	-0.03	-0.08	0.01	2		1.00	-0.45	-0.26	0.32	-0.04	-0.07	0.04
3			1.00	-0.37	-0.46	0.27	0.16	-0.06	3			1.00	-0.23	-0.52	0.34	0.01	-0.05
4				1.00	-0.02	-0.66	0.01	0.16	4				1.00	-0.12	-0.71	0.39	-0.11
5					1.00	0.06	-0.67	-0.01	5					1.00	0.04	-0.71	0.42
6						1.00	0.36	-0.50	6						1.00	-0.10	-0.30
7							1.00	-0.02	7							1.00	-0.53
8								1.00	8								1.00

segmented in 0.9° × 0.9° projective towers read out in three sections in depth. It has a total thickness of 22 radiation lengths and yields a relative energy resolution of $0.18/\sqrt{E} + 0.009$ (E in GeV), for isolated photons. Electrons are identified by their transverse and longitudinal shower profiles in the ECAL and their specific ionization in the TPC. The iron return yoke is instrumented with 23 layers of streamer tubes and forms the hadron calorimeter (HCAL). The latter provides a relative energy resolution for hadrons of $0.85/\sqrt{E}$ (E in GeV). Muons are distinguished from hadrons by their characteristic pattern in HCAL and by the muon chambers, composed of two double-layers of streamer tubes outside HCAL. The two luminosity calorimeters, a silicon-tungsten detector (SiCAL) [17] and a lead/proportional wire sampling calorimeter (LCAL), measure the energy of the scattered beam electrons and cover the angular ranges of $24\,\mathrm{mrad} < \Theta_{\mathrm{tag}} < 58\,\mathrm{mrad}$ and $45\,\mathrm{mrad} < \Theta_{\mathrm{tag}} < 160\,\mathrm{mrad}$. The energy resolution is $\sigma_E/E = 0.34/\sqrt{E}$ for SiCAL and $\sigma_E/E = 0.034 \oplus 0.15/\sqrt{E}$ for LCAL (E in GeV). An energy-flow algorithm combines the information from the tracking detectors and the calorimeters [16]. For each event, the algorithm provides a set of charged and neutral reconstructed particles, called *'energy-flow objects'* in the following.

Studies on the trigger efficiency have been performed indicating a value of 100% over the kinematic region used for this analysis [18]. A conservative estimate for the un-

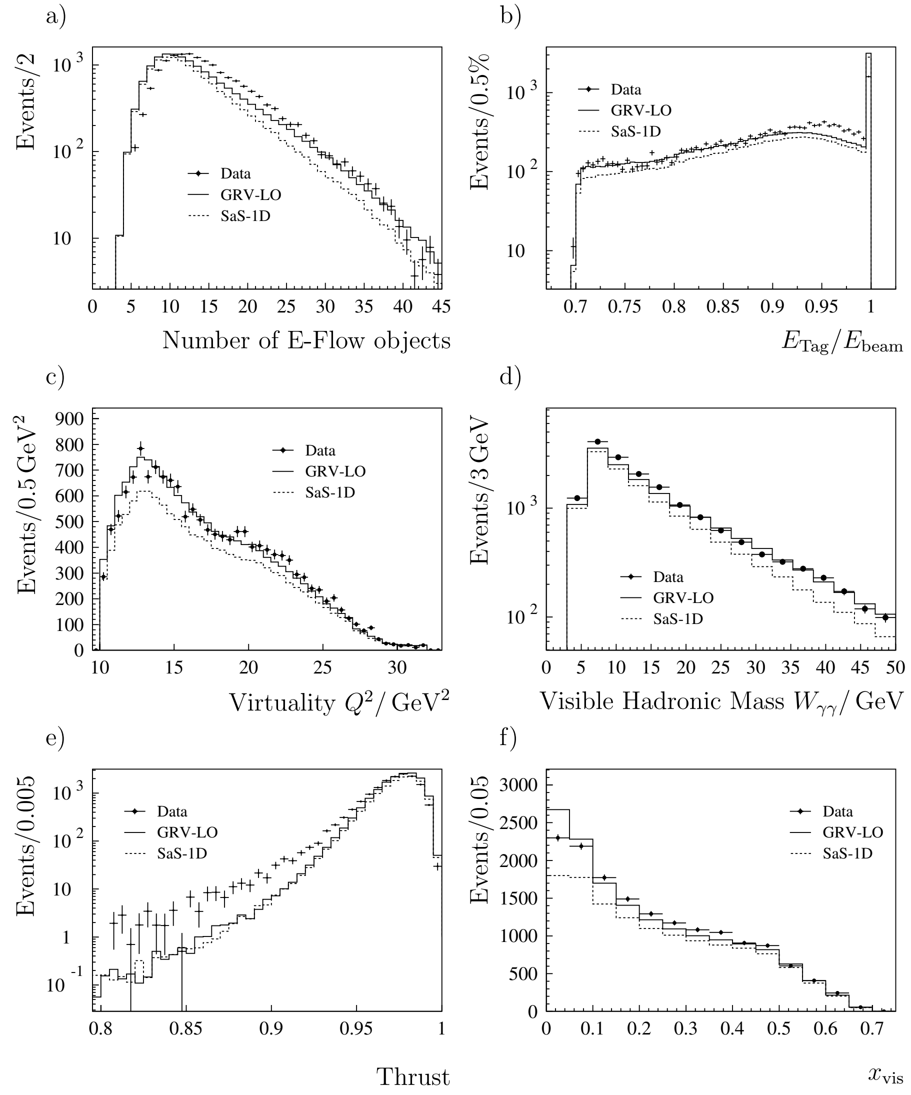

Fig. 3a–f. Comparison of data and Monte Carlo simulations for the sample with $\langle Q^2 \rangle = 17.3\,\mathrm{GeV}^2$. The histograms are HERWIG simulations using a GRV-LO parametrization (solid line) and a SaS-1D set of parameters (dashed line) for the input structure function. ALEPH data with backgrounds subtracted are shown with full errors. The plots show **a** the number of energy-flow objects, **b** the energy of the tagged electron as a fraction of the beam energy, **c** the virtuality Q^2 of the photon radiated from the tagged electron, **d** the visible invariant mass of the hadronic final state, **e** the thrust and **f** the visible Bjorken variable x. All histograms are normalized to the data luminosity

certainty on this has been taken as 5% and 10% for the two upper bins in the Bjorken variable x.

3 Data samples

The data used in this analysis were taken in the years 1998, 1999 and 2000 at different centre-of-mass energies between $\sqrt{s} = 189\,\mathrm{GeV}$ and $\sqrt{s} = 207\,\mathrm{GeV}$. Single tag events are required to contain a single electron detected in the luminosity calorimeters with an energy of at least 70% of the beam energy. Although the silicon calorimeter covers a range from 24 mrad up to 58 mrad, electrons are only detected for $\Theta > 34\,\mathrm{mrad}$ since a tungsten shielding against backscattered synchrotron photons was introduced into its acceptance region in 1996. In order to reject double-tag events where both beam electrons are detected, events with a further energy-flow object in the luminosity calorimeters with more than 40% of the beam energy are excluded. Single-tag events cannot be distinguished from no-tag events with a "fake" tag produced by an off-momentum electron. This background can be suppressed by cuts in the (θ, ϕ) plane for tagged electrons with energy less than 80% of E_{beam} since off-momentum electrons are preferably emitted in the LEP plane. Here ϕ is the azimuthal angle and θ the angle between the scattered electron and the beam direction. The cuts are shown in Fig. 1, from a comparison with Monte Carlo simulation and the analysis of angular distributions the residual background is estimated to be smaller than 1% [19]. In order to eliminate beam gas events, the reconstructed interaction vertex is required to be within 5 cm in the z direction and 1 cm in the radial direction of the nominal interaction point.

The data are analyzed separately for the centre-of-mass energies $\sqrt{s} = 189\,\mathrm{GeV}$, $\sqrt{s} = 196\,\mathrm{GeV}$, $\sqrt{s} = 200\,\mathrm{GeV}$ and $\sqrt{s} = 205 - 207\,\mathrm{GeV}$ because of different background conditions and the different boosts of the hadronic system. The integrated luminosity is listed in Table 1 which also shows the number of selected events and the cuts which define two bins in Q^2. The boundary

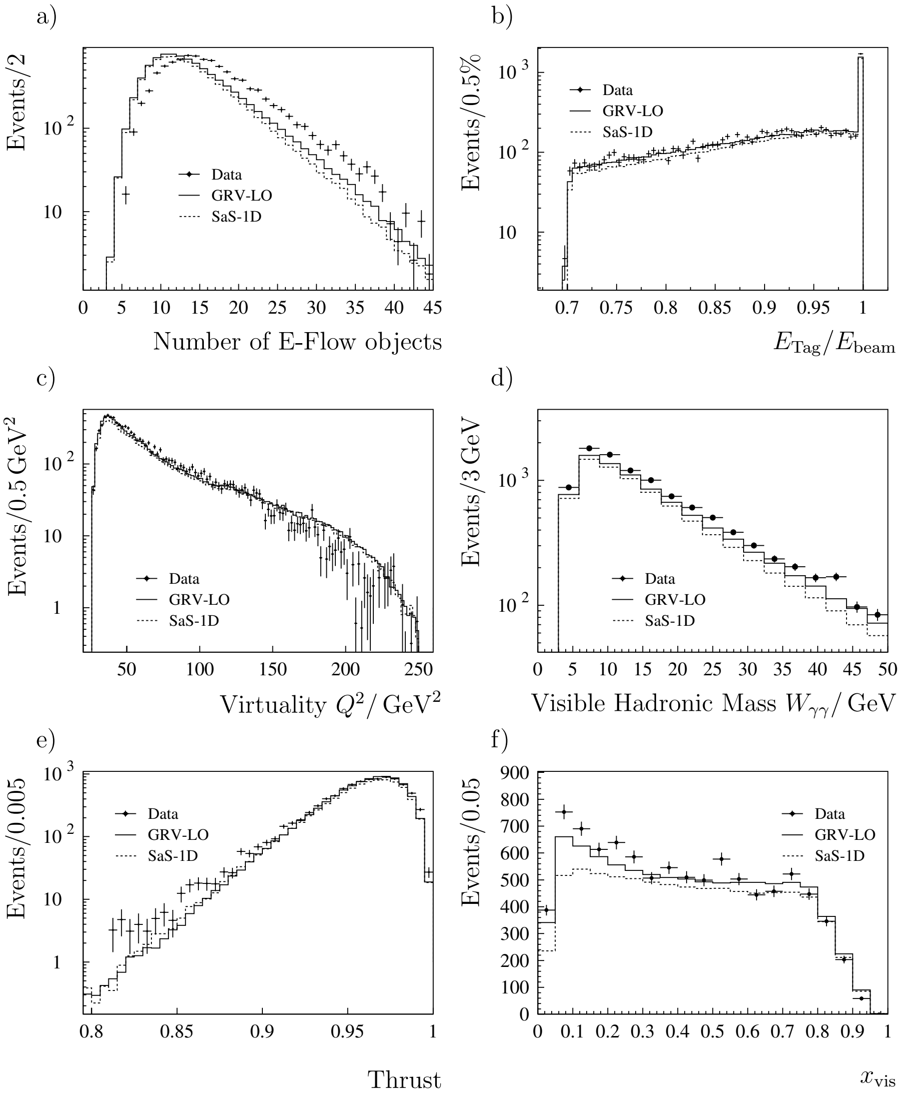

Fig. 4a–f. Distributions of the same variables as shown in Fig. 3, but for the high Q^2 region with $\langle Q^2\rangle = 67.2\,\mathrm{GeV}^2$

between the lower and the upper Q^2 range varies with centre-of-mass energy and is chosen such that migration between the two Q^2-bins is minimized.

The visible hadronic final state is required to consist of at least three charged particles with an invariant mass of at least $3.5\,\mathrm{GeV}/c^2$ in the lower Q^2 region and $3\,\mathrm{GeV}/c^2$ in the upper Q^2 region. Events with particles identified as electrons or muons with an energy of more than 2.5 GeV in the final state are rejected because they are more likely produced in background processes than in the decay chain of hadronic final state particles in $\gamma\gamma$ processes. It has been checked that these cuts do not affect the signal efficiency, e.g. events from open charm production are not rejected. The background from $\gamma\gamma \to \tau^+\tau^-$ as well as $\mathrm{e}^+\mathrm{e}^-$ annihilation events is simulated and subtracted. The contamination from $\gamma\gamma \to l\bar{l}$ is about 4% in the low Q^2 region and 7% in the high Q^2 region. The background from annihilation events is between 0.4% and 1.5%. A detailed list of all investigated background processes can be found in Table 2.

3.1 Unfolding Procedure

In order to determine the structure function F_2^γ it is necessary to measure the differential cross section $\mathrm{d}\sigma/\mathrm{d}x$. Both Q^2 and the invariant mass of the hadronic system are affected by sizeable measurement uncertainties. In particular for low Q^2 the energy resolution of the luminosity calorimeter leads to a relatively poor measurement of the virtuality Q^2. Due to the strong Lorentz boost of the hadronic system the measurement of $W_{\gamma\gamma}$ suffers from the limited acceptance of the detector in the very forward direction. Therefore x is not well determined (Fig. 2) and has to be corrected for these detector effects.

Starting from some sample parametrizations of the structure function, Monte Carlo studies with full detector simulation give a detector-response matrix A which depends only weakly on the parametrization used, but reflects the acceptance and efficiency of the ALEPH detector. The equation

$$A\vec{x}_{\mathrm{true,\,MC}} = \vec{x}_{\mathrm{vis,\,MC}} \tag{5}$$

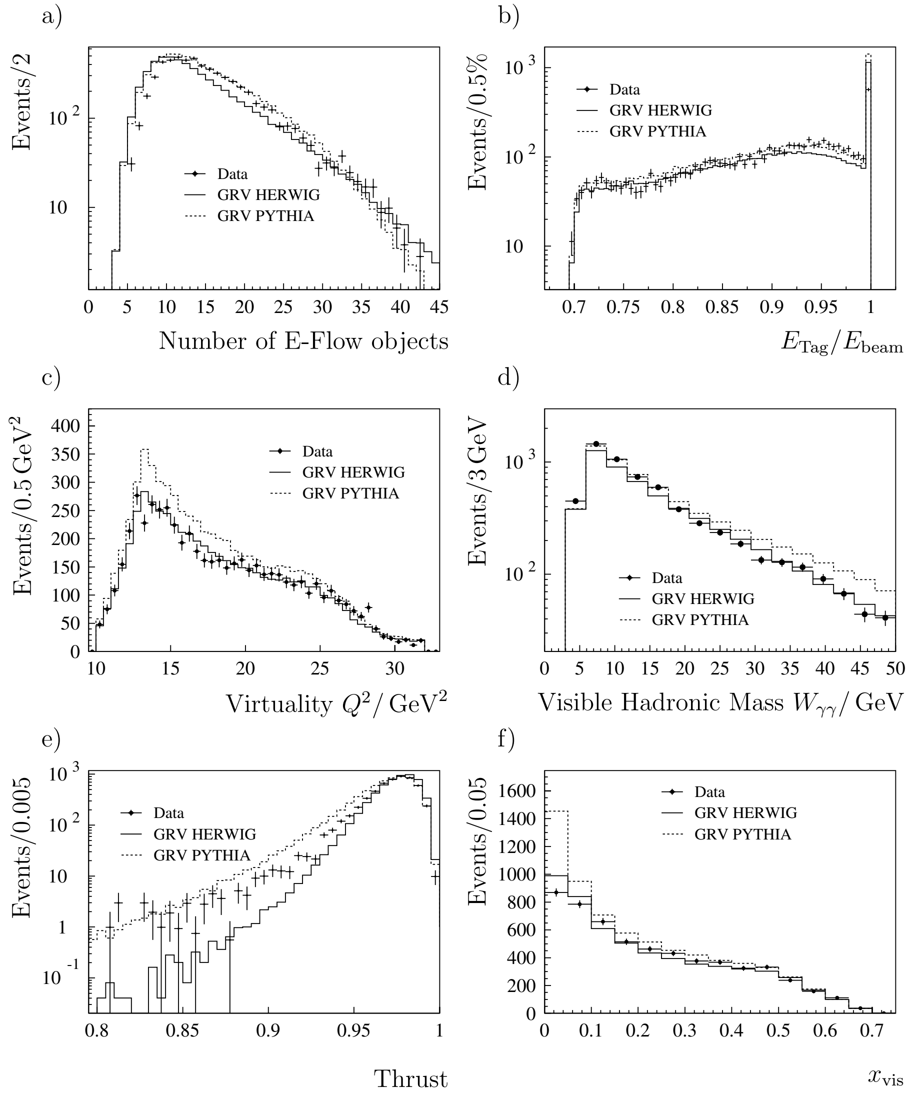

Fig. 5a–f. The distribution of the same variables are shown as in Fig. 3, with the data compared to Monte Carlo simulations from the two different generators HERWIG (solid line) and PYTHIA (dashed line). In both cases the GRV-LO parametrization is used. $\langle Q^2 \rangle = 17.3\,\mathrm{GeV}^2$

connects the reconstructed x spectrum $\vec{x}_{\mathrm{vis,\,MC}}$ with the generated x spectrum $\vec{x}_{\mathrm{true,\,MC}}$. The bin boundaries have been chosen such that the number of events in each bin of the true x spectrum is roughly constant for a Monte Carlo sample that contains all centre-of-mass energies and two different parametrizations of F_2^γ. It has been checked that the results are sufficiently insensitive to reasonable variations of the bin boundaries.

For the low Q^2 range the x spectrum extends from $x = 2 \cdot 10^{-3}$ to $x = 0.7$ and is divided into eight bins. The same number of bins is used for x between $6 \cdot 10^{-3}$ and 0.96 for the high Q^2 region. In principle the true unfolded x distribution could now be found for each measured $\vec{x}_{\mathrm{vis,\,data}}$ by inverting (5):

$$\vec{x}_{\mathrm{true,\,data}} = A^{-1}\vec{x}_{\mathrm{vis,\,data}} \tag{6}$$

Because of the special topology of the events and the reduced detector acceptance, the matrix A represents a so called ill-conditioned system. As a consequence it turns out that small fluctuations in the measured distribution lead to an unfolded $\vec{x}$ which differs strongly from the true $\vec{x}$ and has large statistical errors. Therefore a bias has to be introduced in order to obtain a regularized distribution. The treatment of ill-conditioned problems and regularization has been widely discussed in the mathematical literature and a recent review can be found in [20]. In this analysis a standard Tikhonov unfolding is used as described in [21]. Here the equation

$$(\alpha I + A^T A)\vec{x}_{\mathrm{unf,\,data}}(\alpha) = A^T \vec{x}_{\mathrm{vis,\,data}} \tag{7}$$

is solved for a particular choice of the regularization parameter α. Since the measurement of the lowest and the highest x bin is considered to be not as reliable as for the central region, the six inner bins are used to find the regularization parameter that gives the smallest statistical error for the unfolded spectrum, such that $A\vec{x}_{\mathrm{unf}}$ is consistent with the observed distribution within the statistical errors of the measurement. The approximation error introduced by the parameter α will be discussed later. The advantage of this method lies in the linear nature of the algorithm and an intuitive strategy to estimate the error which is introduced by regularization.

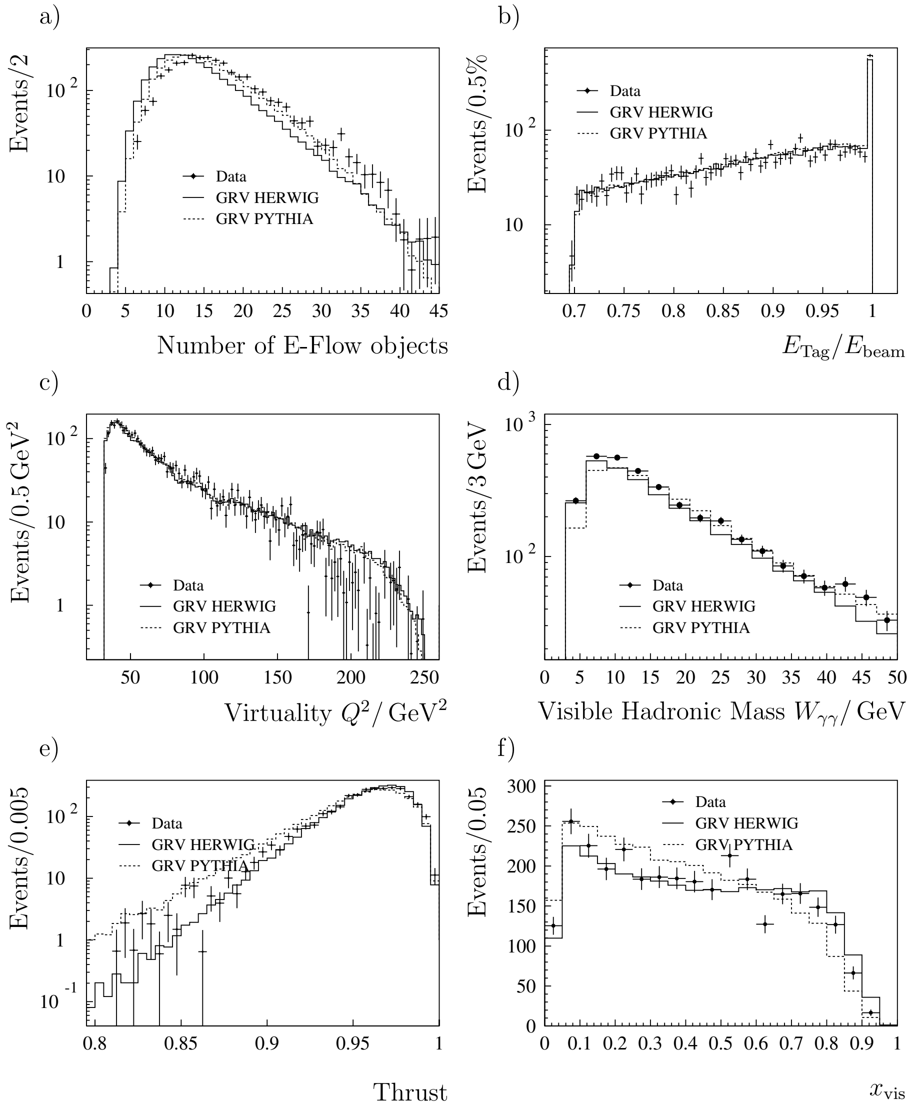

Fig. 6a–f. Distributions of the same variables as shown in Fig. 5 but for the high Q^2 region with $\langle Q^2 \rangle = 67.2\,\mathrm{GeV}^2$

Parametrizations giving reasonable descriptions of global event variables are used to construct the detector-response matrix. A comparison between data and Monte Carlo simulation is shown in Figs. 3 and 4. In this analysis simulated events from the HERWIG6.2 program [22] are used to build the matrix A, although some observables such as multiplicity of the energy-flow objects and the thrust of the event are not well reproduced and are described better by the PYTHIA6.1 generator [23]. However, those quantities that go into the analysis directly, i.e. Q^2, W and x, are in better agreement with the measured data for the HERWIG simulation. In Figs. 5 and 6 a comparison between the different Monte Carlo generators and data can be found. For each centre-of-mass energy, samples of one million events are generated for each of the parametrizations GRV-LO [7,8] and SaS1D [12] implemented via PDFLIB [24]. The uncertainties of the detector-response matrix due to the limited Monte Carlo statistics cannot be neglected. They are calculated by a full error propagation depending on the regularization parameter α and are included in the systematic errors for the final results [25].

The correction is such that the unfolded distribution gives an estimate of the true x distribution in the given Q^2 range. The cuts in E_{tag}, Θ_{tag} and the cuts against leptonic and other background were not applied for the "truth" spectrum. The only requirement, apart from the cut in Q^2, is that $W_{\gamma\gamma}$ be at least 2.5 GeV, since below that value the Monte Carlo simulation is not considered to be fully reliable.

For the construction of the detector-response matrix it is important to handle events that migrate into the Q^2 region of interest. Events which are generated outside the investigated interval of Q^2, but are reconstructed inside, have to be subtracted like background, whereas migration out of the considered Q^2 region can easily be treated as inefficiency. A model-dependent uncertainty is introduced because this background due to the finite Q^2 resolution has to be simulated. The GRV-LO parametrization is used to simulate this background which amounts to about 4% of

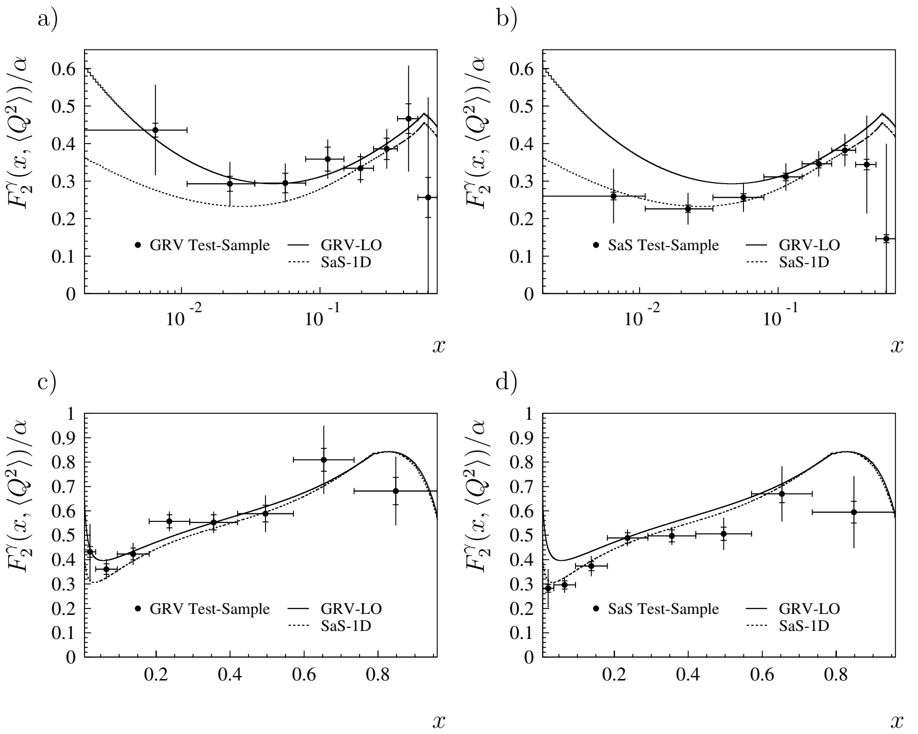

Fig. 7a–d. The unfolded structure function $F_2^\gamma(x,\langle Q^2\rangle)/\alpha$ for Monte Carlo test samples of the same size of the data sample used in this analysis. The test samples are subject to exactly the same analysis procedure as the data. The outer error bars give the total uncertainty, the inner marks show the statistical uncertainty only. The systematics include all contributions except fragmentation

Table 4. Measured values of F_2^γ and their uncertainties. The total error in column three is a quadratic sum of the statistical and systematic errors, given in column four and five. The last four columns show contributions to the systematic uncertainties from the approximation error due to regularization, fragmentation uncertainty, the model dependence of the detector-response matrix and other effects as described in the text

$\langle Q^2\rangle = 17.3\,\mathrm{GeV}^2$								
x Bin	F_2^γ	Uncertainties						
		Total	Stat.	System.	Approx.	Frag.	Model	others
0.0020 - 0.0110	0.43	0.116	0.016	0.115	0.017	0.108	0.010	0.035
0.0110 - 0.0338	0.27	0.051	0.014	0.049	0.006	0.045	0.005	0.018
0.0338 - 0.0787	0.35	0.044	0.015	0.041	0.008	0.032	0.005	0.024
0.0787 - 0.1487	0.35	0.032	0.015	0.028	0.007	0.003	0.003	0.027
0.1487 - 0.2429	0.39	0.037	0.016	0.034	0.003	0.007	0.009	0.032
0.2429 - 0.3624	0.46	0.045	0.018	0.041	0.024	0.018	0.003	0.027
0.3624 - 0.5074	0.40	0.150	0.021	0.149	0.136	0.003	0.017	0.058
0.5074 - 0.7000	0.18	0.236	0.019	0.235	0.227	0.007	0.009	0.060

$\langle Q^2\rangle = 67.2\,\mathrm{GeV}^2$								
x Bin	F_2^γ	Uncertainties						
		Total	Stat.	System.	Approx.	Frag.	Model	others
0.0060 - 0.0362	0.57	0.148	0.027	0.145	0.018	0.142	0.005	0.026
0.0362 - 0.0950	0.43	0.048	0.027	0.039	0.009	0.012	0.017	0.032
0.0950 - 0.1811	0.47	0.050	0.029	0.041	0.011	0.017	0.014	0.033
0.1811 - 0.2907	0.50	0.044	0.031	0.031	0.009	0.007	0.003	0.028
0.2907 - 0.4204	0.60	0.052	0.036	0.038	0.013	0.007	0.010	0.033
0.4204 - 0.5714	0.66	0.086	0.038	0.077	0.007	0.064	0.014	0.041
0.5714 - 0.7356	0.65	0.138	0.055	0.126	0.029	0.086	0.041	0.077
0.7356 - 0.9600	0.66	0.150	0.060	0.137	0.069	0.076	0.022	0.089

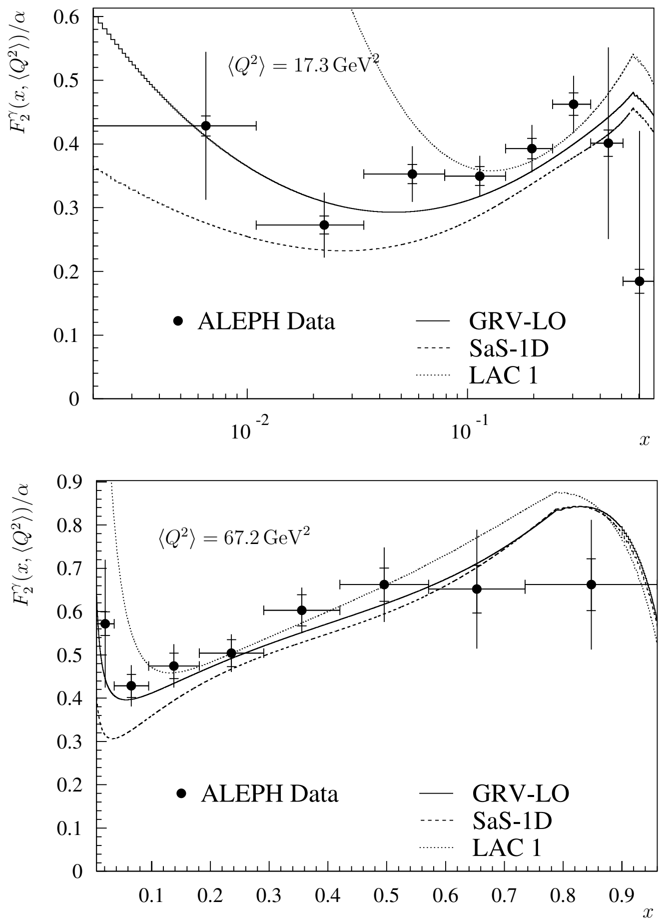

Fig. 8. The measured values of F_2^γ/α. The results for all centre-of-mass energies are combined using the luminosity of the data samples as weight. Inner error bars indicate statistical errors only. The measurement is compared to three different parametrizations

the selected data in the low Q^2 bin and 2% in the upper Q^2 bin. It has been checked that simulations based on other parametrizations give almost no difference in the unfolded result.

3.2 Extraction of F_2^γ

The unfolded spectrum $\mathrm{d}\sigma/\mathrm{d}x$ allows the calculation of the measured structure function F_2^γ. The proportionality factor between F_2^γ and $\mathrm{d}\sigma/\mathrm{d}x$ is calculated from Monte Carlo simulation using theoretical models:

$$F_2^\gamma(x, \langle Q^2\rangle)_{\mathrm{meas}} = \frac{\mathrm{d}\sigma/\mathrm{d}x(x, \langle Q^2\rangle)_{\mathrm{meas}}}{\mathrm{d}\sigma/\mathrm{d}x(x, \langle Q^2\rangle)_{\mathrm{model}}} \cdot F_2^\gamma(x, \langle Q^2\rangle)_{\mathrm{model}}$$

Here the parametrizations from GRV-LO and SaS-1D have been used as reference models. Studies with Monte Carlo samples show that the unfolding method applied here reproduces the input structure function correctly, as shown in Fig. 7.

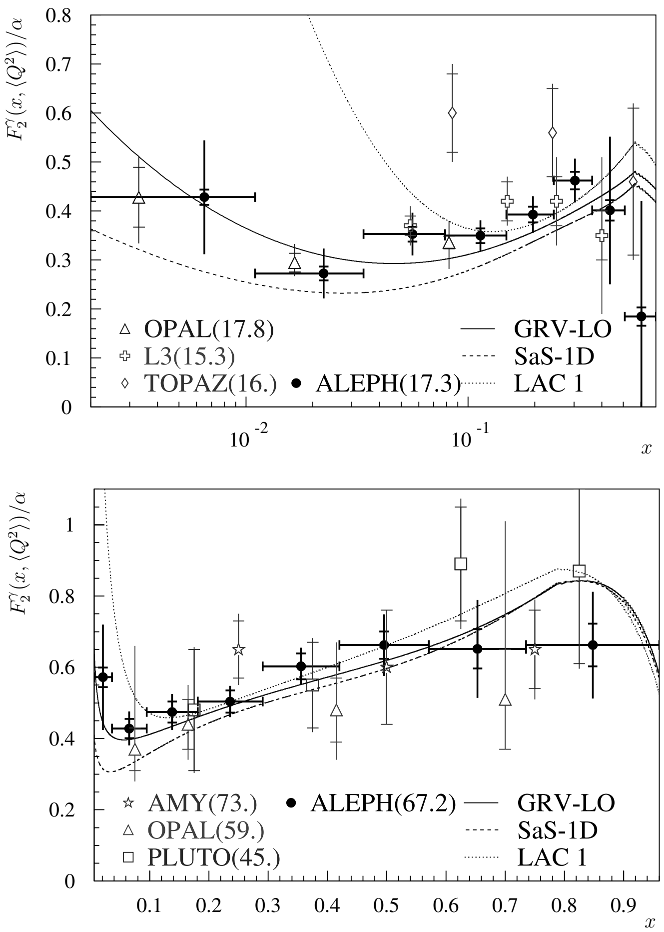

Fig. 9. The values of F_2^γ/α from this analysis compared to earlier measurements for similar values of $\langle Q^2\rangle$. Inner error bars indicate statistical errors only if available from the publications. The parametrizations GRV-LO, SAS-1D and LAC1 are shown as well

3.3 Systematic uncertainties

An important contribution to the systematic uncertainty comes from the regularization in the unfolding procedure. The regularization of the system (7) is equivalent to a modification of the detector response. Depending on the strength of the regularization this gives an uncertainty that has to be taken into account. This cannot be calculated from data and has to be estimated from a model since the true x spectrum has to be known. Here Monte Carlo samples with GRV-LO and SaS-1D parametrizations are used. Although the number of observed events is larger for higher x, this approximation uncertainty dominates the error in that region compared to low x. The reason for that is that usually a large fraction of the hadronic invariant mass $W_{\gamma\gamma}$ is not reconstructed. Therefore low x events might be seen at higher x values which is taken into account by the detector simulation, however, events with high x are frequently lost completely. This inefficiency causes the large approximation uncertainty since the detector-response matrix becomes almost singular in that region.

Table 5. Comparison between the measured results presented in this analysis and various theoretical predictions which are calculated with the PDFLIB program. The fifth column gives the order of the approximation to which the parametrization is calculated (Leading Order (LO) or Next to Leading Log-Approximation(NLL))

PDFLIB	Λ_{QCD}	Q^2_{min}	Name of set	Approx.	χ^2/n.d.f. for $\langle Q^2 \rangle =$		Ref.
set	/MeV	/GeV^2		order	17.3 GeV^2	67.2 GeV^2	
3/1/1	380	10	DO-G set 1	LO	47	6.4	[3]
3/1/2	440	10	DO-G set 2	NLL	5.8	0.3	
3/2/1	400	1	DG-G set 1	LO	0.2	0.03	[4]
3/2/2	400	1	DG-G set 2	LO	0.2	0.1	
3/2/3	400	10	DG-G set 3	LO	0.2	0.03	
3/3/1	200	5	LAC-G set 1	LO	2.4	0.4	[5]
3/3/2	200	5	LAC-G set 2	LO	2.0	0.4	
3/3/3	200	5	LAC-G set 3	LO	0.2	0.04	
3/3/4	200	5	GAL-G	LO	0.9	3.6	
3/4/1	200	5.3	GS-G HO	NLL	0.3	0.1	
3/4/2	200	5.3	GS-G LO set 1	LO	0.3	0.1	
3/4/3	200	5.3	GS-G LO set 2	LO	0.2	0.1	
3/4/4	200	5.3	GS-G-96 HO	NLL	0.4	0.1	
3/4/5	200	5.3	GS-G-96 LO	LO	0.2	0.04	
3/5/1	200	0.3	GRV-G HO	NLL	0.3	0.1	[7,8]
3/5/2	200	0.3	GRV-G HO	NLL	0.6	0.1	
3/5/3	200	0.25	GRV-G LO	LO	0.3	0.03	
3/5/4	200	0.6	GRS-G LO	LO	0.3	0.04	
3/6/1	200	2	ACFGP-G set HO	NLL	0.3	0.1	
3/6/2	200	2	ACFGP-G set HO-mc	NLL	0.1	0.03	
3/6/3	200	2	AFG-G set HO	NLL	0.4	0.2	
3/8/1	400	4	WHIT-G 1	LO	0.2	0.02	[11]
3/8/2	400	4	WHIT-G 2	LO	0.6	0.01	
3/8/3	400	4	WHIT-G 3	LO	0.9	0.03	
3/8/4	400	4	WHIT-G 4	LO	0.5	0.1	
3/8/5	400	4	WHIT-G 5	LO	1.7	0.1	
3/8/6	400	4	WHIT-G 6	LO	2.5	0.1	
3/9/1	200	0.36	SaS-G 1D (V. 1)	LO	0.2	0.1	[12]
3/9/2	200	0.36	SaS-G 1M (V. 1)	LO	0.3	0.1	
3/9/3	200	4	SaS-G 2D (V. 1)	LO	0.2	0.03	
3/9/4	200	4	SaS-G 2M (V. 1)	LO	0.2	0.1	
3/9/5	200	0.36	SaS-G 1D (V. 2)	LO	0.2	0.1	
3/9/6	200	0.36	SaS-G 1M (V. 2)	LO	0.3	0.1	
3/9/7	200	4	SaS-G 2D (V. 2)	LO	0.2	0.03	
3/9/8	200	4	SaS-G 2M (V. 2)	LO	0.2	0.1	

The largest systematic uncertainty in the low x region results from different fragmentation models used in the Monte Carlo simulation. The analysis has been repeated using a Monte Carlo sample produced with the PYTHIA 6.1 generator. Half the difference between the unfolded results from both models is taken as a systematic uncertainty.

The dependence of the detector-response matrix on the parton-density function (p.d.f.) that was used to generate it, is considered as a further effect. The unfolding is done separately with matrices from two different p.d.f.'s and the mean of both results is taken as the final result. Half the difference of the two results is taken as a systematic uncertainty.

The energy and momentum calibration of the detector was changed artificially by ±2% for all particles in the hadronic system. The effect has only minor influence on the results ($< 2\%$) since the major uncertainty in the measurement of the hadronic system comes from lost tracks rather than from the resolution of the tracking devices and calorimeters.

The virtuality of the target photon is small but not vanishing. In the HERWIG Monte Carlo generator it is produced with $\langle P^2 \rangle \approx 0.082\,\mathrm{GeV}^2$. The shape of the vir-

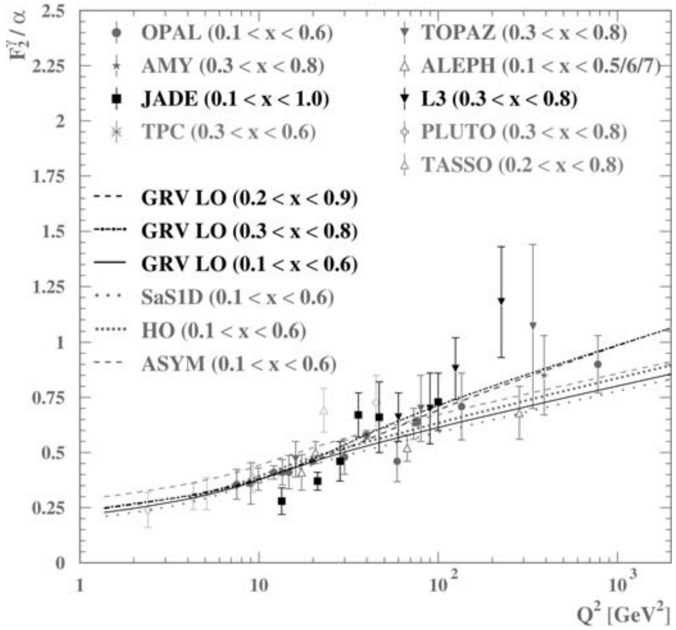

Fig. 10. Q^2 evolution for medium values of x measured by different experiments. The result from this analysis is included for $\langle Q^2 \rangle = 17.3\,\mathrm{GeV}^2$ and $0.1 < x < 0.5$ and for $\langle Q^2 \rangle = 67.2\,\mathrm{GeV}^2$ and $0.1 < x < 0.7$. Details about the parametrisations are given in [14] where this plot, here updated with our measurement, was taken from

tuality spectrum of the quasi-real target photon can be taken as simply the ρ pole or from the generalized vector meson dominance model. The effect on the result can then be computed with the GALUGA program [26]. The uncertainty amounts to 2-5%, depending slightly on x.

All systematic uncertainties and the statistical error are added in quadrature to obtain the total error.

4 Results and conclusions

The measured structure function F_2^γ is shown in Fig. 8 for both regions in Q^2. The unfolded spectra from all different centre-of-mass energies are combined. The measurement integrates over the photon virtuality P^2. Although the P^2 spectrum is not limited by an explicit cut, 90% of all events are below 1 GeV. The inner marks on the error bars indicate the statistical errors, the whole error bars show systematic and statistical errors added in quadrature. Due to the unfolding procedure and the properties of the detector-response matrix the measured points of the structure function are highly correlated. The correlation matrices are given in Table 3.

The curves show three examples of different parametrizations taken from PDFLIB, however the statistical significance of this measurement is too small to distinguish between different models. Overall the shape of the GRV-LO and SaS1D parametrizations are reproduced, but the absolute value of the measurement is slightly higher. At low x values, where the structure function is sensitive to the gluon content, the gluon-rich parametrization LAC [5] is not consistent with this measurement. For a comparison with additional models, the χ^2 values have been calculated and listed in Table 5. Most of the predictions are in rather good agreement. This is mainly due to the large systematic uncertainties. The calculations are done for a charm quark mass of $m_c = 1.4\,\mathrm{GeV}/c^2$.

Since the hadronic structure function of the photon was first measured by the PLUTO collaboration [27], many experiments have made contributions so that data are now available for F_2^γ in a wide range of Q^2. In Fig. 9 the ALEPH results from this analysis are shown together with measurements which are comparable in $\langle Q^2 \rangle$ from OPAL ($\langle Q^2 \rangle = 17.8\,\mathrm{GeV}^2$) [28], TOPAZ ($\langle Q^2 \rangle = 16\,\mathrm{GeV}^2$) [29], L3 ($\langle Q^2 \rangle = 15.3\,\mathrm{GeV}^2$) [30] and OPAL ($\langle Q^2 \rangle = 59\,\mathrm{GeV}^2$) [31], AMY ($\langle Q^2 \rangle = 73\,\mathrm{GeV}^2$) [32] and PLUTO ($\langle Q^2 \rangle = 45\,\mathrm{GeV}^2$) [33].

The Q^2 dependence of the structure function cannot be fitted to the measurement, since only two bins in Q^2 are considered. Usually the mean values of F_2^γ are compared for a central x range. For the bins in Q^2 used here the values

$$\begin{aligned} &F_2^\gamma(0.1 \le x \le 0.5, \langle Q^2 \rangle = 17.3\,\mathrm{GeV}^2) \\ &\quad = 0.41 \pm 0.01\ (\mathrm{stat.}) \pm 0.08\ (\mathrm{sys.}), \\ &F_2^\gamma(0.1 \le x \le 0.7, \langle Q^2 \rangle = 67.2\,\mathrm{GeV}^2) \\ &\quad = 0.52 \pm 0.01\ (\mathrm{stat.}) \pm 0.06\ (\mathrm{sys.}). \end{aligned}$$

are obtained. In Fig. 10 the results are shown in comparison to other experiments.

Acknowledgements. We wish to thank our colleagues in the CERN accelerator divisions for the successful operation of LEP. We are indebted to the engineers and technicians in all our institutions for their contribution to the excellent performance of ALEPH. Those of us from non-member countries thank CERN for its hospitality.

References

1. V. M. Budnev, I. F. Ginzburg, G. V. Meledin, V. G. Serbo, Phys. Rep. C **15**, 181–282 (1975)
2. E. Witten, Nucl. Phys. B **120**, 189–202 (1977)
3. D. W. Duke, J. F. Owens, Phys. Rev. D **26**, 1600 (1982)
4. M. Drees, K. Grassie, Z. Phys. C **28**, 451 (1985)
5. H. Abramowicz, K. Charchula, A. Levy, Phys. Lett. B **269**, 458 (1991)
6. L. E. Gordon, J. K. Storrow, Nucl. Phys. B **489**, 405 (1997)
7. M. Glück, E. Reya, A. Vogt, Phys. Rev. D **45**, 3986 (1992)
8. M. Glück, E. Reya, A. Vogt, Phys. Rev. D **46**, 1974 (1992)
9. P. Aurenche et al., Z. Phys. C **56**, 589 (1992)
10. P. Aurenche, J.-P. Guillet, M. Fontannaz, Z. Phys. C **64**, 621 (1994)
11. K. Hagiwara, M. Tanaka, I. Watanabe, T. Izubuchi, Phys. Rev. D **51**, 3197 (1995)
12. G. A. Schuler, T. Sjöstrand, Z. Phys. C **68**, 607 (1995)
13. M. Krawczyk, "Structure Functions for the Virtual and Real Photons." In: A. J. Finch (Editor): Proceedings of PHOTON2000. Ambleside, England: AIP Conference Proceedings Vol. 571, Melville, New York (2000)

14. R. Nisius, "The photon structure from deep inelastic electron-photon scattering", Phys. Rep. **332**, 165–317 (2000); updated figures available at: http://www.mppmu.mpg.de/~nisius/welcomeaux/struc.html
15. ALEPH Collaboration, "ALEPH: a detector for electron-positron annihilation at LEP", Nucl. Instrum. and Methods A **294**, 121 (1990)
16. ALEPH Collaboration, "Performance of the ALEPH detector at LEP", Nucl. Instrum. and Methods A **360**, 481 (1995)
17. B. Mours et al., "The design, construction and performance of the ALEPH silicon vertex detector", Nucl. Instrum. and Methods A **379**, 121 (1996)
18. ALEPH Collaboration, "Measurement of the hadronic photon structure function at LEP I for Q^2 values between 9.9 and 284 GeV^2", Phys. Lett. B **458**, 152 (1999)
19. G. Prange, "Messung des hadronischen Wirkungsquerschnitts doppelt markierter 2-Photon Ereignisse", Fachbereich Physik, Universität Siegen, Ph.-D. Thesis (2001)
20. H. W. Engl, M. Hanke, A. Neubauer, "Regularization of Inverse Problems", Dordrecht: Kluwer Academic Publishers, 1996
21. R. Kress, "Numerical Analysis", Graduate Texts in Mathematics, New York, Berlin: Springer-Verlag, 1997
22. G. Corcella et al., CERN-TH/2000-284; http://hepwww.rl.ac.uk/theory/seymour/herwig/
23. T. Sjöstrand, Comp. Phys. Commun. **82**, 74 (1994); http://www.thep.lu.se/~torbjorn/Pythia.html
24. H. Plothow-Besch, "PDFLIB Proton, Pion and Photon Parton Density Functions, Parton Density Functions of the Nucleus and α_s Calculations", Users's Manual, Version 8.04, CERN-ETT/TT (2000)
25. J. Heß, "Measurement of the Hadronic Photon Structure Function $F_2^\gamma(x,Q^2)$ in Two-Photon Collisions", Fachbereich Physik, Universität Siegen, Ph.-D. Thesis (2002)
26. G. A. Schuler, Comp. Phys. Commun. **108**, 279 (1998)
27. PLUTO Collaboration, "First Measurement of the Photon Structure Function F_2", Phys. Lett. **107B**, 168–172 (1981)
28. OPAL Collaboration, "Measurement of the low-x behaviour of the photon structure function F_2^γ", Eur. Phys. J. C **18**, 15–39 (2000)
29. TOPAZ Collaboration, "Measurement of the photon structure function F_2^γ and jet production at TRISTAN", Phys. Lett. B **332**, 477–487 (1994)
30. L3 Collaboration, "The Q^2 evolution of the hadronic photon structure function F_2^γ at LEP", Phys. Lett. B **447**, 147–156 (1999). The XIth International Workshop on Gamma-Gamma Collisions, Egmond aan Zee, 10–15 May 1997, World Scientific, Singapore, 1998, 26–30
31. OPAL Collaboration, "Measurement of the Q^2 Evolution of the Photon Structure Function F_2^γ", Phys. Lett. B **411**, 387–401 (1997)
32. AMY Collaboration, "A measurement of the photon structure function F_2", Phys. Lett. B **252**, 491–498 (1990)
33. PLUTO Collaboration, "Measurement and QCD Analysis of the Photon Structure Function $F_2^\gamma(x,Q^2)$", Nucl. Phys. B **281**, 365–380 (1987)